Scalar field induced oscillations of relativistic stars and gravitational collapse

Florian Siebel and José A. Font
Max-Planck-Institut für Astrophysik, Karl-Schwarzschild-Strasse 1, D-85741 Garching, Germany

Philippos Papadopoulos
School of Computer Science and Mathematics, University of Portsmouth, Portsmouth PO1 2EG, United Kingdom
(Received 2 August 2001; published 21 December 2001)

We study the interaction of massless scalar fields with relativistic stars by means of fully dynamic numerical simulations of the Einstein-Klein-Gordon perfect fluid system. Our investigation is restricted to spherical symmetry and the stars are approximated by relativistic polytropes. Studying the nonlinear dynamics of isolated compact objects is very effectively performed within the characteristic formulation of general relativity, in which the spacetime is foliated by a family of outgoing light cones. We are able to compactify the entire spacetime on a computational grid and simultaneously impose natural radiative boundary conditions and extract accurate radiative signals. We study the transfer of energy from the scalar field to the fluid star. We find, in particular, that depending on the compactness of the stellar model, the scalar wave forces the star either to oscillate in its radial modes of pulsation or to undergo gravitational collapse to a black hole on a dynamical time scale. The radiative signal, read off at future null infinity, shows quasinormal oscillations before the setting of a late time power-law tail.

DOI: 10.1103/PhysRevD.65.024021 PACS number(s): 04.25.Dm, 04.40.Dg, 95.30.Lz, 97.60.Lf

I. INTRODUCTION

Obtaining reliable estimates for gravitational wave signals emitted from the collapse of massive stars is one of the key motivations for numerical relativity. The strength of actual astrophysical sources is still under investigation, as the relevance of such sources for the first and second generation of interferometric detectors depends on the details of signal amplitude and frequency, but also on the occurrence rates (for a current view, see [1]). In any case, relativistic collapse is a fundamental physical process, and the development of relevant computational procedures has been a long steady process over the past three decades (see, e.g., [2–4]; see also [5] and references therein). In contrast with a Newtonian approximation, where the computational problem is well defined and attention can be devoted to astrophysical details [5,6], there is no consensus as to what is the optimal, or at least adequate, framework for developing relativistic simulations.

We will use here the so-called *characteristic* formulation of general relativity [7,8]. The formalism has been developed specifically for addressing ambiguities concerning gravitational radiation and is well adapted to handle the propagation of signals. It allows for spacetime compactification, which avoids problems due to the artificial reflection of the fields at outer boundaries. In addition, it allows for the extraction of physically relevant global quantities, such as the News function and the Bondi mass. Nevertheless, the computation of the dynamics of *sources* of signals is a separate issue altogether, which has not been addressed in this early work. The framework for computing a complete spacetime within the characteristic approach has been laid out in [9] and more explicitly in [10]. The translation of this framework into a computational tool for vacuum spacetimes, in any dimensions, has been a largely successful process (see [11] and references therein).

There are some noteworthy issues. First, the domain of applicability of the approach is limited to configurations in which the set of light cones that forms the backbone of the coordinate system does not fold itself into caustics. This puts a limit, for example, on the type of binary system that can be studied. Second, to obtain a complete *regular* spacetime (in contrast with a black hole spacetime), one must include in the computational domain the vertex of the light cones. This involves regularity conditions (and for explicit integration methods, severe time-step restrictions), which at present have been resolved only up to axisymmetric configurations [12]. Nevertheless, the approach has remarkable economy and stability, which makes it a good candidate for studies of isolated relativistic objects emitting gravitational radiation. For the simulation of realistic astrophysical sources, one would have to include suitable matter models. It was demonstrated in [13] that the modern techniques of high-resolution shock-capturing schemes for solving the equations of relativistic fluid dynamics can be effectively integrated within this framework. A separate study, implementing this new approach, focused on the gravitational radiation properties of an accreting black hole [14].

This work is the first example of the use of characteristic numerical relativity for the study of dynamical relativistic star spacetimes, collapse and generation of radiative signals. The present numerical study is performed in spherical symmetry and uses a self-gravitating, massless, scalar field. The latter serves as a simple matter model which mimics gravitational waves. It has been used frequently to study global properties of spacetimes, black hole formation and the properties of radiative signals. This includes the interaction of scalar waves and black holes (e.g. [15,16]) and especially the emergence of power-law tails [17–20], which arise from late time backscattering of the scalar field at the exterior spacetime geometry [21]. There are few studies of the interaction of scalar fields with fluid stellar objects. Recently [22] analyzed the scattering of scalar fields off boson stars and the

emergence of critical solutions for this setup. They found that the scalar field can make the boson star either collapse to a black hole or disperse its mass to infinity.

Time-dependent simulations of the scattering of gravitational wave packets off relativistic stars, as a means of computing the frequency spectrum of the relativistic star (see, e.g., [23] for a recent review), have been studied by Allen *et al.* [24] for polytropic equations of state (EOS's), and by Ruoff [25] for more realistic EOS's. Such simulations were performed using linear perturbation techniques. Pavlidou *et al.* [26] studied the radiative falloff of scalar fields in neutron star spacetimes, using (idealized) analytic, constant density relativistic star models and assuming stationarity for the fluid and the geometry.

In the present work we investigate the nonlinear dynamics of relativistic stars interacting with scalar fields. We are especially interested in the following questions: How does a stable relativistic star react when it interacts with the scalar field? Can the scalar field induce gravitational collapse? What is the result of the interaction on the scalar field? In order to answer these questions we obtain numerically spherically symmetric evolutions of the Einstein-Klein-Gordon perfect fluid system. We study the reflection of finite scalar wave packets off relativistic stars for a series of models, parametrized, for a given polytropic EOS of polytropic index $n=1$, by the central density. Our study focuses on the dynamics of the system during the interaction, both the generation of nonlinear fluid oscillations and the gravitational collapse of the fluid component to a black hole.

The paper is organized as follows. Section II describes the basic mathematical foundations of our approach. In Sec. III, we discuss the numerical techniques and the implementation used in the simulations. In Sec. IV, we present several numerical tests of the algorithms, aimed at assessing the correct implementation of the different code components: the hydrodynamic evolution, the scalar field evolution, and the metric solver. Section V describes the actual numerical investigation of the interaction between the relativistic stars and the scalar field. Finally, Sec. VI summarizes our findings. Throughout the paper we use geometrized units $G=c=1$ and further assume that $M_{\odot}=1$. Greek indices run from 0 to 3.

II. MATHEMATICAL FRAMEWORK

We consider a general spherically symmetric spacetime with a two component stress energy tensor of a perfect fluid and a scalar field, $T^{\mu\nu}=T_F^{\mu\nu}+T_\Phi^{\mu\nu}$. The geometry of our setup follows the lines of the Tamburino-Winicour formalism [9], in particular as it is applied in regular spacetimes, where the foliation of light cones emanates from a freely falling central observer [10].

A. Einstein equations

By adopting the Bondi-Sachs [7,8] form of the metric element in spherical symmetry,

$$ds^2=-\frac{e^{2\beta}V}{r}du^2-2e^{2\beta}dudr+r^2(d\theta^2+\sin\theta^2 d\phi^2), \tag{1}$$

the spacetime geometry is completely described by the two functions $\beta(u,r)$ and $V(u,r)$.

A sufficient set of Einstein equations for obtaining the spacetime development are grouped as

$$G_{ur}=\kappa T_{ur}, \tag{2}$$

$$G_{rr}=\kappa T_{rr}, \tag{3}$$

$$G_{uu}|_\Gamma=\kappa T_{uu}|_\Gamma, \tag{4}$$

where the u coordinate is defined by the level surfaces of a null scalar (i.e., a scalar u satisfying $\nabla^\mu u\nabla_\mu u=0$). The r coordinate is chosen to make the spheres of rotational symmetry have area $4\pi r^2$. The x^2,x^3 coordinates in this geometry are simply taken to be the angular coordinates (θ,ϕ) propagated along the generators of the null hypersurface, i.e., they parametrize the different light rays on the null cone. With our choice of units the constant κ is simply $\kappa=8\pi$. The first two Einstein equations, Eqs. (2) and (3), contain only radial derivatives and are to be integrated along each null surface. The last equation (4) is a *conservation* condition, satisfied on the vertex of the null cones Γ due to the regularity conditions. We choose Γ to be a timelike geodesic which coincides with the origin of a relativistic star at $r=0$. Equation (3) may be substituted for by the equivalent expression $g^{AB}R_{AB}=8\pi g^{AB}(T_{AB}-g_{AB}T/2)$, where $R_{\mu\nu}$ is the Ricci tensor and the indices (A,B) run over the angular coordinates x^2,x^3.

Using the line element and Eqs. (2) and (3) the β and V hypersurface equations are given by

$$\beta_{,r}=2\pi r T_{rr}, \tag{5}$$

$$V_{,r}=e^{2\beta}[1-4\pi r^2(g^{AB}T_{AB}-T)]. \tag{6}$$

The comma in the above equations indicates, as usual, partial differentiation. Boundary conditions for $(\beta(u)_\Gamma, V(u)_\Gamma)$, needed for the radial integrations, are provided by imposing regularity at the origin, where the coordinate system is assumed to be a local Fermi system, leading to $\beta=O(r^2)$, $V=r+O(r^3)$. By imposing such conditions at the origin, the lapse of coordinate time du is related to the corresponding lapse of "retarded time" $d\tau$ measured by distant observers at $r\to\infty$ by

$$d\tau=e^{2H}du, \tag{7}$$

where $H=\lim_{r\to\infty}\beta$.

B. Scalar field equations

The dynamics of a scalar field Φ is governed by the minimally coupled Klein-Gordon equation in spherical symmetry,

$$\nabla_\mu\nabla^\mu\Phi=0, \tag{8}$$

where ∇_μ is the covariant derivative. The corresponding stress energy tensor is given by

$$T_\Phi^{\mu\nu}=\nabla^\mu\Phi\nabla^\nu\Phi+Lg^{\mu\nu} \tag{9}$$

where L is the massless scalar field Lagrangian ($2L=-\nabla_\mu\Phi\nabla^\mu\Phi$). Using a characteristic foliation, Eq. (8) takes the form

$$2(r\Phi_{,u})_{,r}=\frac{1}{r}(rV\Phi_{,r})_{,r}. \tag{10}$$

In terms of the intrinsic 2-metric of the (u,r) submanifold,

$$\eta_{CD}dx^C dx^D=-e^{2\beta}du\left(\frac{V}{r}du+2dr\right), \tag{11}$$

where the indices (C,D) run over the coordinates (u,r), Eq. (10) reduces to

$$\Box^{(2)}g=\frac{e^{-2\beta}g}{r}\left(\frac{V}{r}\right)_{,r}, \tag{12}$$

where $g=r\Phi$ and $\Box^{(2)}$ is the D'Alembertian operator associated with η_{CD}.

C. Hydrodynamic equations

The evolution of the fluid is determined by the local conservation laws of stress energy and density current:

$$\nabla_\mu T_F^{\mu\nu}=0, \tag{13}$$

$$\nabla_\mu(\rho u^\mu)=0, \tag{14}$$

where $T_F^{\mu\nu}$ is the stress energy tensor of a perfect fluid,

$$T_F^{\mu\nu}=\rho h u^\mu u^\nu+pg^{\mu\nu}. \tag{15}$$

All quantities in the above expression have their usual meanings: ρ is the rest mass density, $h=1+\varepsilon+p/\rho$ is the specific enthalpy, ε is the specific internal energy and p is the pressure of the fluid. Moreover, u^μ is the four-velocity which satisfies the normalization condition $g_{\mu\nu}u^\mu u^\nu=-1$.

Following [13], after introducing the definitions $D=\rho u^0$, $S^r=T_F^{0r}$ and $E=T_F^{00}$, the fluid equations can be cast into a first-order flux-conservative, hyperbolic system for the state vector $\mathbf{U}=(D,S^r,E)$:

$$D_{,u}+F^{r0}_{,r}=-(\ln\sqrt{-g})_{,u}D-(\ln\sqrt{-g})_{,r}F^{r0}, \tag{16}$$

$$S^r_{,u}+F^{r1}_{,r}=-(\ln\sqrt{-g})_{,u}S^r-(\ln\sqrt{-g})_{,r}F^{r1}-\Gamma^r_{\mu\nu}T_F^{\mu\nu}, \tag{17}$$

$$E_{,u}+F^{r4}_{,r}=-(\ln\sqrt{-g})_{,u}E-(\ln\sqrt{-g})_{,r}F^{r4}-\Gamma^u_{\mu\nu}T_F^{\mu\nu}, \tag{18}$$

where $\sqrt{-g}=r^2\sin\theta e^{2\beta}$ is the square root of the determinant of the four dimensional metric and $\Gamma^\alpha_{\mu\nu}$ are the Christoffel symbols. The precise form of the vector of fluxes $\mathbf{F}$ can be obtained by using Eqs. (13),(14) (see also [13]). The explicit relations between the primitive variables $\mathbf{w}=(\rho,\varepsilon,u^r)$ and the conserved variables $\mathbf{U}=(D,S^r,E)$, for a perfect fluid EOS, $p=(\Gamma-1)\rho\varepsilon$, where Γ is the adiabatic index of the fluid, are given in [13].

With the above definitions, the metric Eqs. (5),(6) read, for the combined stress energy tensor of a fluid-scalar field system,

$$\beta_{,r}=2\pi r[\rho h(u_r)^2+(\Phi_{,r})^2], \tag{19}$$

$$V_{,r}=e^{2\beta}[1-4\pi r^2(\rho h-2p)]. \tag{20}$$

Following [27] we express the hydrodynamic quantities on the right-hand side of Eqs. (19),(20) solely in terms of the conserved hydrodynamic quantities $\mathbf{U}$. This avoids the additional iterations required, when using explicit algorithms, to integrate the hypersurface equations for the metric consistently with the normalization condition for the fluid.

In summary, the initial value problem consists of Eqs. (4), (12), (16)–(18), and (19),(20), the scalar field initial data $\Phi(r,u_0)$ and initial and boundary data for the fluid variables (ρ,ε,u^r) on the initial slice Σ_0 (at time u_0). Those equations and initial data are sufficient for obtaining a global solution to the problem.

D. Global quantities

Making use of the characteristic formulation of general relativity and covering the infinite range of the radial coordinate with a finite grid allows us to refer to some global quantities of the spacetime such as the Bondi mass and the news function. Apart from their physical relevance, these quantities can be used in global tests of our numerical evolutions, as we will show below.

Instead of extracting the Bondi mass directly at future null infinity we use the expression

$$M=4\pi\int_0^\infty r^2e^{-2\beta}T_{ru}dr \tag{21}$$

for the Bondi mass at time u in our numerical implementation. Similarly, the news can be rewritten as [15]

$$N=\frac{1}{2}e^{-2H}\int_0^\infty\frac{V}{r}\Phi_{,r}dr. \tag{22}$$

With these definitions, global energy conservation can be established:

$$M(u)-M(0)=\int_0^u-4\pi N(\hat{u})^2e^{2H(\hat{u})}d\hat{u}. \tag{23}$$

III. NUMERICAL IMPLEMENTATION

In order to study the interaction of the scalar field and the relativistic star in a global spacetime we use nonequidistant grids for the radial coordinate r. Furthermore, to avoid dealing with complicated stencils in the numerical implementation, we make use of the following procedure, generalizing previous implementations in characteristic numerical relativity (see, e.g., [12]): Starting with an equidistant grid in the

coordinate $x \in [0,1]$, we allow for a general coordinate transformation $r=r(x)$. Using the chain rule we rewrite the partial derivatives appearing in the above equation with

$$(),_r = (),_x \frac{dx}{dr}, \tag{24}$$

thus effectively rewriting all our equations in the coordinate x. Unless otherwise stated we use the relation

$$r = \frac{15x}{1-x^4} \tag{25}$$

for all computations presented in this work. Using such a coordinate transformation, the repartition of grid points in the coordinate r is almost equidistant for small radii and gets infinitely sparse for $x \to 1$, which corresponds to future null infinity $\mathcal{J}^+$.

We use a second order Runge-Kutta method to solve the metric equations (19) and (20). To determine the equilibrium models for the fluid configuration, we also use the Runge-Kutta method to solve the Tolman-Oppenheimer-Volkoff equations, formulated on a null hypersurface as in [13].

The integration of the evolution equation for the scalar field Eq. (12) [or equivalently Eq. (10)] proceeds with the specification of initial data $\Phi(u_0,r)$ on the initial null cone u_0. For the characteristic evolution we have used and compared two different algorithms. The first procedure is based upon the construction of a null parallelogram built up from incoming and outgoing radial characteristics [28]. In this procedure one needs first to determine the right hand side of Eq. (12) at the center of the parallelogram to the desired order of accuracy. Then, an integral relation between this source term and the values of g at the four corners of the parallelogram—which do not necessarily have to coincide with grid points—has to be employed in order to compute the scalar field at that corner of the parallelogram lying next to the grid point that is to be updated. Suitable interpolations then give the scalar field at the new grid point to second order accuracy. The second alternative procedure we have implemented to solve the scalar field equation is based on a direct discretization of Eq. (10) using a second order, finite difference, nondissipative algorithm discussed in [29].

Because of the stencils of the two algorithms, we cannot use them at the origin, where regular behavior of the scalar field as $\Phi = a + br + cr^2$ is assumed. The linear term introduces a kink at the origin, but this is necessary in our foliation—as can be seen from the analytic solution for the wave equation in Minkowski space consisting of an ingoing and an outgoing wave. Note that the scalar field enters the metric only through Eq. (19), thus respecting the regularity conditions at the origin. Substituting this ansatz into Eq. (10) and grouping those terms with the same powers of r we find that $a_{,u}=b$, $b_{,u}=1.5c$. Extracting the coefficients a,b and c on the null cone u_0, we update a and b to obtain the scalar field at the first two grid points of the new hypersurface, which then allows us to start the marching procedure along the null hypersurface with either of the two algorithms described above.

By experimenting with both algorithms, we found that, on the one hand, the scheme based upon a direct discretization of the wave equation is more accurate in the long-term behavior in the interior of the numerical domain. This was relevant to resolve the late time falloff behavior of the scalar field, as we describe below in Sec. V. On the other hand, the algorithm based upon the null parallelogram is superior close to future null infinity, where we regularized the equations following the work of [12]. Therefore, for the results presented in this work we have used a ''hybrid algorithm'' in which a direct discretization of Eq. (10) is used in the interior of the computational domain and the parallelogram algorithm is used close to future null infinity $\mathcal{J}^+$.

Concerning the numerical integration of the system of hydrodynamic equations, its hyperbolic mathematical character allows for a solution procedure based on the computation of (local) Riemann problems at each cell interface of the numerical grid. At cell i the state vector $\mathbf{U}$ is updated in time (from u^n to u^{n+1}) using a conservative algorithm

$$\mathbf{U}_i^{n+1} = \mathbf{U}_j^n - \frac{\Delta u}{\Delta x}(\hat{\mathbf{F}}_{i+1/2} - \hat{\mathbf{F}}_{i-1/2}) + \Delta u \mathbf{S}_j, \tag{26}$$

where the numerical fluxes, $\hat{\mathbf{F}}$, are evaluated at the cell interfaces according to some particular *flux formula* which makes explicit use of the full spectral decomposition of the system. For our particular formulation of the hydrodynamic equations such characteristic information was presented in [13].

In more precise terms the hydrodynamics solver of our code uses a second order Godunov-type algorithm, based on piecewise linear reconstruction procedures at each cell interface [30] and the Harten–Lax–van Leer–Einfeldt (HLLE) approximate Riemann solver [31,32]. General information on such schemes in relativistic hydrodynamics can be found, e.g., in [33] and references therein.

IV. CODE TESTS

We now describe results of code calibration procedures. We present a range of tests in some detail, motivated by the central role of the present developments in future higher-dimensional algorithms. The assessment of the numerical implementation is achieved primarily by comparing with independent physical results and performing global energy conservation tests.

A. Null cone evolution of stable stars

As a first step to validate the algorithms we start by studying their ability to maintain the equilibrium of initially stable relativistic star models. For this purpose we perform long-term simulations of such initial data and analyze the stability of the code. Furthermore, we use these evolutions to compute the frequencies of the radial modes of pulsation. We compare the frequencies obtained with our nonlinear code to results of linear evolutions from perturbation theory.

For all simulations presented in this paper the star models are approximated by a polytropic EOS, defined by $p=K\rho^\Gamma$, with polytropic constant $K=100$ and adiabatic exponent Γ

$\equiv 1+1/n=2$. Hence, the index of the polytrope is $n=1$. For the simulation presented in this section we choose the model with central density $\rho_c=1.5\times10^{-3}$ (recall that we are using units in which $G=c=M_\odot=1$). This model is located in the stable branch of the central density—total mass—diagram. When evolving this model with our numerical code we are able to maintain a stable equilibrium for thousands of light-crossing times of the star without any sign of numerical instabilities.

To validate the code further we compute the frequencies of radial pulsation modes. To achieve this, in the present Eulerian framework, we must allow the star to (radially) contract and expand during the evolution. Following [34] (see also [35]), we surround the star with a few zones representing an artificial ''atmosphere'' filling an otherwise vacuum region. The density in this atmosphere is set to sufficiently small values such that its presence does not affect the dynamics of the system. Typical values we choose are 10^{-7}–10^{-8} times the central density of the star. Furthermore, to avoid any numerical problems due to (shock) heating in the atmosphere (the fluid in those zones is not in equilibrium and, therefore, it will collapse/accrete onto the star), we follow the recipe described in [34] and enforce adiabatic evolution (by using the polytropic EOS) in the atmosphere and in the outer layers of the relativistic star (comprising the outermost 10 grid points). After each time step, if the density has fallen below 1.5 times the density of the atmosphere, the hydrodynamic quantities are reset to their atmosphere values. The innermost location where this procedure is done defines the radius of the star. As described in more detail in the next section the above values of the atmosphere density are small enough to guarantee conservation of energy despite the artificial resetting procedure.

When evolving our stellar model in time, we find small deviations around the equilibrium values due to the discretization errors. As a result, the star oscillates in a superposition of radial modes. Figure 1 shows the radial velocity at half stellar radius for the above model as a function of the retarded time measured by distant observers. This simulation was performed with a grid of 800 zones covering the complete radial domain. This amounts to using about half of the available grid in resolving the relativistic star. (We choose this resolution here to allow for comparisons with the results of Sec. V, where we resolve the scalar field as well). As shown in [35] one can use such evolutions to obtain the frequencies of the excited modes of pulsation of the star by simply Fourier transforming those data. In general, however, the excitation of the different modes by the truncation error of the numerical schemes may not be sufficient to accurately determine the mode frequencies. The truncation error of the discretization scheme introduces at each grid point a nonstationary perturbation. The pointwise nature of those perturbations implies that the spectrum of induced oscillations is fairly broad, essentially covering all wave numbers representable on a given grid resolution, but with varying power in different regimes. In order to excite the relevant modes more strongly, we perturb the density of the equilibrium models with an explicit function $\rho=\rho_0+A\rho_c\sin(\pi r/R)$, where R denotes the radius of the star (see Table I below)

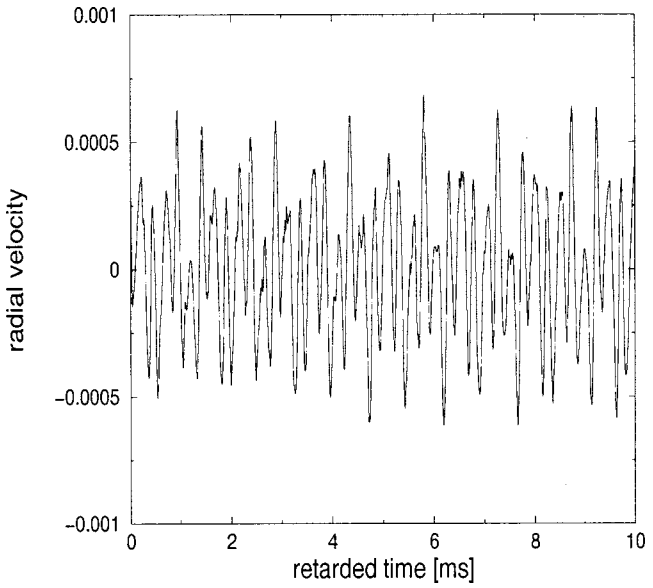

FIG. 1. Time evolution of the radial velocity u^x at the half radius of the star. The stellar model has a central density $\rho_c=1.5\times10^{-3}$. The oscillations are essentially undamped for the evolution shown, which reflects the small viscosity of the hydrodynamic scheme employed.

and ρ_0 is the density of the unperturbed star. The typical amplitude we use for this perturbation is $A=10^{-6}$.

Figure 2 shows the frequencies of the fundamental mode and the first two overtones obtained by a Fourier transform of the radial velocity profiles. The dashed vertical lines in this plot were obtained using a code [36] that solves the linearized perturbation equations. The agreement between the two codes is very good. Similar results were obtained for a relativistic polytrope with $\rho_c=2.8\times10^{-3}$, for which the fundamental mode is already rather small, the star being close to the unstable branch. We note that the code is able to track considerably higher overtones as well, but for the sake of clarity in the comparison it is sufficient to show only the first two harmonics.

B. Scalar field dynamics in a regular spacetime

In this section we present results aimed to validate the numerical implementation of the Einstein-Klein-Gordon solver. For this purpose we investigate the reflection of a

TABLE I. Equilibrium properties of the $K=100$, $n=1$ relativistic star models in units in which $c=G=M_\odot=1$. The entries are as follows: ρ_c is the central density, M and R are the mass and radius of the star, respectively, and $C=2M/R$ is the compactness parameter.

ρ_c (10^{-3})	M	R	$C=2M/R$
1.5	1.47	9.26	0.317
2.2	1.60	8.45	0.379
2.8	1.63	7.91	0.412
2.9	1.64	7.84	0.418
3.0	1.64	7.76	0.423

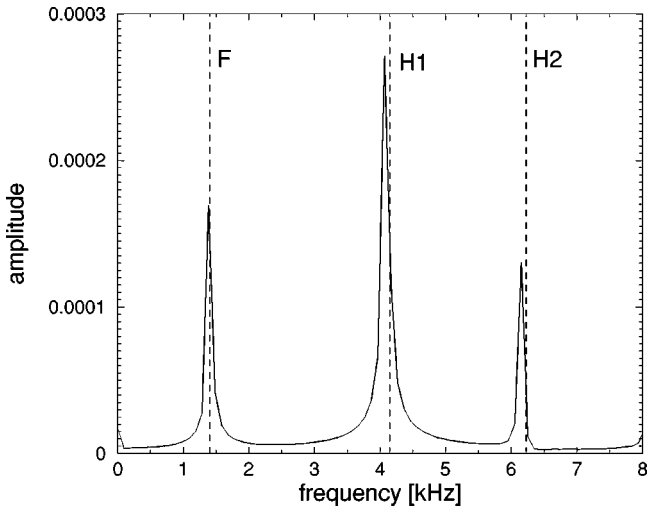

FIG. 2. Fourier transform of the time evolution shown in Fig. 1. The peaks in the Fourier transform indicate the mode frequencies of the fundamental radial mode (around $f=1.4$ kHz) and the first two harmonics. The relativistic star model has a central density $\rho_c = 1.5\times10^{-3}$. The dashed vertical lines indicate the corresponding frequencies obtained with a perturbative (linear) code. The units on the y axis are arbitrary.

scalar field at the origin of the coordinate system, turning off the hydrodynamics module of the code. The initial data for the scalar field packet are

$$\Phi_0 = 2\times10^{-3} e^{-(r-14)^2}. \tag{27}$$

The location of this Gaussian pulse is chosen in such a way that, if superposed on the relativistic star spacetimes of the previous section, the scalar field data would initially lie outside the relativistic star. Evolving these data, the initial pulse approaches the origin, is reflected, and radiates away, leaving behind Minkowski space. Such a sequence can be followed in Fig. 3, for a simulation employing a grid of 800 zones. We

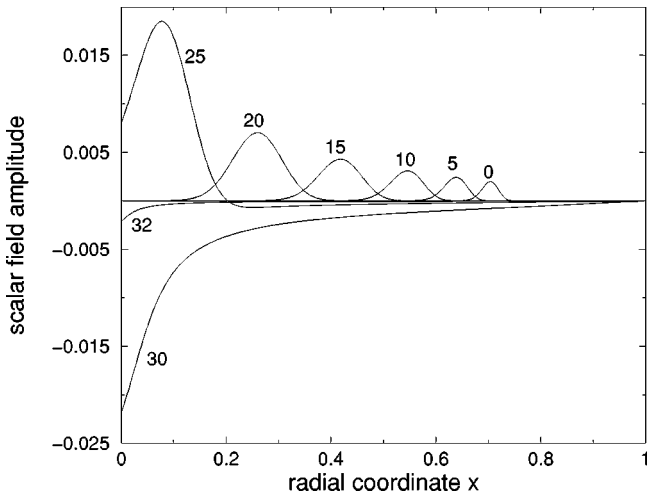

FIG. 3. Radial profiles of the scattering of a scalar field off the origin of the coordinate system. The number labels refer to the time coordinate u. For times $u \geqslant 35$ the pulse has completely radiated away, leaving Minkowski spacetime behind.

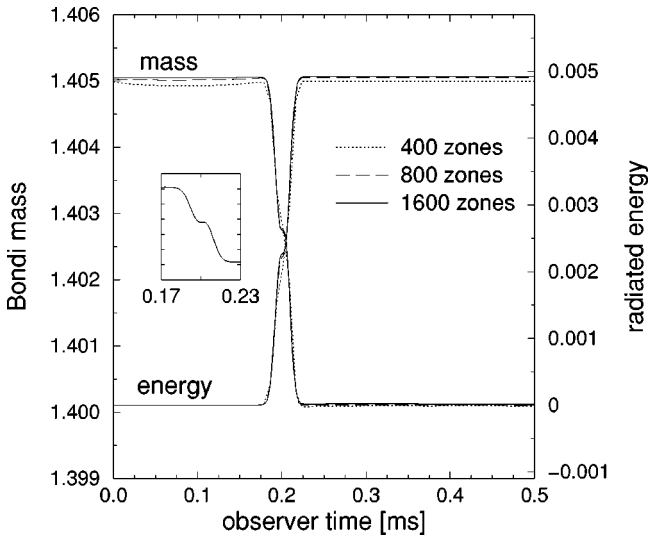

FIG. 4. Bondi mass of the spacetime and total radiated energy of the scalar field as a function of retarded time for different resolutions. At the beginning, the scalar field contributes to the Bondi mass of the spacetime ($1.405M_\odot$), before the Bondi mass drops in a small time interval, when the main part of scalar field mass (about $5\times10^{-3}M_\odot$) is emitted to future null infinity $\mathcal{J}^+$. As the sum of the two curves is constant, the energy is globally conserved (with a relative error of about 5×10^{-6} for the run with 1600 zones.). The mass drops in two steps around 0.2 ms, which can be seen from the magnified figure obtained for the case of 1600 zones.

note the stability and smoothness of the solution, both at the origin and at $\mathcal{J}^+$. By evaluating global energy conservation, according to Eq. (23), after the pulse has reflected off the origin, we find that the energy is conserved (as expected) to second order accuracy. As an aside we note that by simply changing the origin treatment in the code, it is possible to study the evolution of a scalar field outside a spherical black hole. We performed such a simulation finding agreement with the results of [19].

C. Global energy conservation

We consider now the full set of equations and prescribe initial data consisting of a scalar field component given by Eq. (27), together with a stable, equilibrium, relativistic star model with initial central density $\rho_c = 1.28\times10^{-3}$, $K=100$ and $\Gamma=2$. We calculate for this stellar model a total mass of $1.4M_\odot$, in agreement with [35]. We perform simulations of the scalar field scattering off the relativistic star, focusing our study in this section on the assessment of the global energy conservation properties of the coupled numerical algorithm. A comprehensive study of the dynamics of the scattering is deferred to Sec. V.

Figure 4 shows the Bondi mass of the relativistic star–scalar field spacetime as a function of retarded time, combined with the total mass of the scalar field radiated away to null infinity. As one can clearly see from this figure, the spacetime is losing mass exactly at the rate that energy is radiated to null infinity by the scalar field.

By computing Eq. (23) at a fixed retarded time of $\tau = 0.5$ ms for different grid resolutions, we find that our code

conserves the energy globally with a convergence rate that lies between 1 and 2. The fact that the convergence rate now drops below second order is, however, to be expected, since the approximate Riemann solver used for the integration of the hydrodynamic equations is only (locally) first order accurate at discontinuities (i.e., the surface of the star) and at local extrema (i.e., the center of the star) (see the related discussion in [35]). Nevertheless, for the highest resolution we have used, 2000 radial grid points, the relative error in the energy conservation is of the order of 2×10^{-6} for this very dynamical simulation.

At first sight the decay of the scalar field mass in two steps as shown in Fig. 4 around 0.2 ms seems surprising. However, looking at the radiated power $dM_B/du=-4\pi e^{-2H}(\lim_{r\to\infty}g_{,u})^2$ and approximating the solution of Eq. (12) by the solution in Minkowski space $g(u,r)=f(u/2+r)-f(u/2)$, where f is determined by the initial profile with suitable falloff behavior for large radii, the radiated power reads $dM_B/du=-\pi e^{-2H}f'(u/2)^2$. Hence the radiated power as a function of time measures the square of the derivative of the initial scalar field profile.

V. DYNAMICS OF SCALAR FIELD–RELATIVISTIC STAR INTERACTIONS

In this section we present our main results concerning the scattering of a scalar field pulse off a relativistic star. As mentioned before, we use $n=1$ relativistic polytropes as the underlying star model. All configurations we construct are stable and are characterized by increasing central densities and compactness. Their basic properties are summarized in Table I.

On the initial outgoing light cone, in addition to the fluid data we introduce a scalar field component in the shape of a Gaussian pulse according to Eq. (27), thus fixing the pulse amplitude, width and location. For these initial data there is no significant initial overlap between the star and the scalar field which then makes it possible to associate a specific initial mass with each one of the matter fields.

In our exploration of the parameter space, we use the central density as the only free parameter, maintaining a single polytropic EOS and fixing the profile and amplitude of the scalar field. This is clearly a severe restriction in the parameter space of the scattering problem. Nevertheless, we choose this particular setup since we are interested in investigating the relativistic effects of the interaction, where the scalar field has a strong impact on the dynamics of the relativistic star. A detailed analysis of the whole parameter space is beyond the scope of this work.

When evolving in time the initial data, the scalar field travels inwards, enters the relativistic star and is finally reflected at the origin of the coordinate system. Contrary to the Einstein-Klein-Gordon system in vacuum (which was briefly discussed in Sec. IV B), the presence of the star and its associated potential well may give rise to a phase of multiple reflections of the scalar field. This, in turn, is reflected in the existence of quasiperiodic signals (trapped modes), as discussed, e.g., by [26], before its energy is radiated away. Furthermore, our relativistic star models have been chosen conveniently close to the maximum of the stability curve at about $\rho_c=3.2\times10^{-3}$. Depending on the compactness of the neutron star onto which the wave pulse impacts, the stars are forced to either oscillate violently, or collapse to a black hole on a dynamical time scale. Figure 5 shows the spacetime diagram for the least compact relativistic star model of our sample, with $\rho_c=1.5\times10^{-3}$. For this model, the scalar field is able to force the star to contract and to expand, pulsating radially, as can clearly be identified in the varying location of the star's radius (the vertical solid line in Fig. 5).

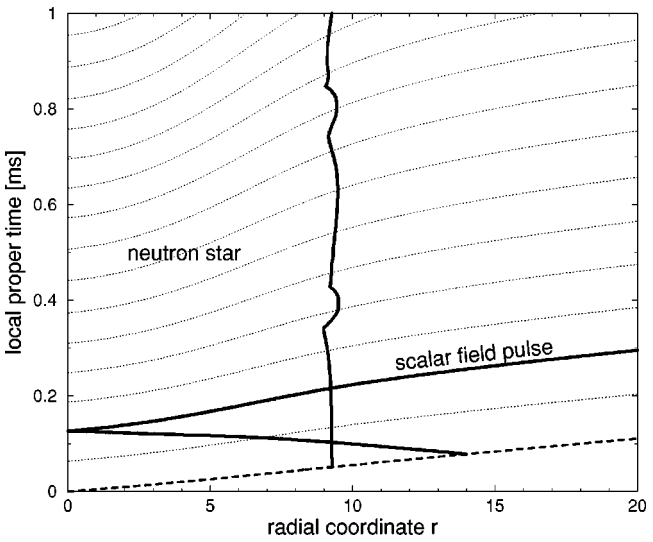

FIG. 5. Spacetime diagram of the reflection of a Gaussian scalar field pulse off a relativistic star ($K=100$, $n=1$ and $\rho_c=1.5\times10^{-3}$). The diagram focuses in the strong field region but was obtained from a global simulation of the spacetime. The dotted curves covering the whole diagram are outgoing light cones, which bend due to the spacetime curvature (the thicker dashed line corresponds to the initial light cone). The scalar field pulse, initially located at $r=14$, travels inward, enters the relativistic star and is reflected at the origin of the coordinate system (the solid line corresponds to the maximum value of the scalar field). The interaction with the scalar field triggers the oscillation of the relativistic star, which can be seen from the vertical solid line of varying location in the diagram, which indicates the radius of the star.

Figure 6 displays the time evolution of the central density of the different relativistic stars in our setup. The solid lines correspond to the relativistic star–scalar field system. Correspondingly, the dashed horizontal lines indicate the evolution of the equilibrium relativistic star models *without* the presence of the scalar field. As already mentioned the initial fluid configurations are stable. The evolution is characterized by the appearance of small-amplitude oscillations associated with the radial modes of pulsation of the star (which are too small to be seen in the figure). On the other hand, all relativistic star–scalar field models with initial central density below 2.8×10^{-3} also oscillate around the stable equilibrium model. The oscillation frequencies of the two least compact models correspond to the frequencies calculated in the linear regime, even though the amplitude of the oscillations is now much larger due to transfer of energy from the scalar field. This is no longer the case for the model with a central density of $\rho_c=2.8\times10^{-3}$. For this model, which is close to the

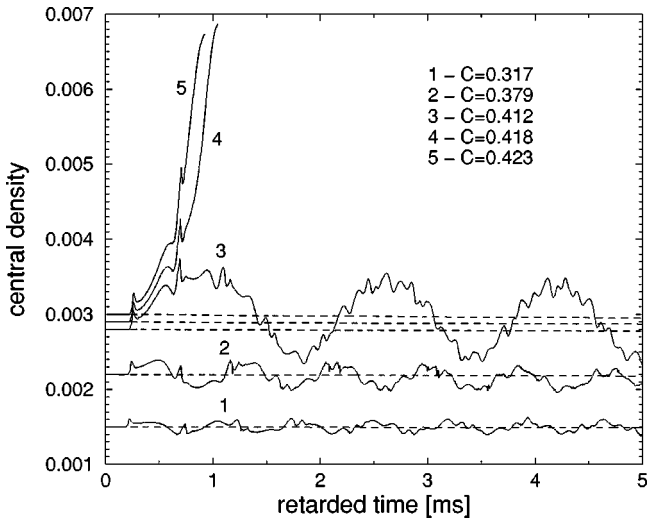

FIG. 6. Central density of the relativistic stars interacting with the scalar field as a function of retarded time. The curves are labeled according to the stellar compactness in Table I. The three less compact models, with $\rho_c \leqslant 2.8\times10^{-3}$, oscillate strongly around their equilibrium value after interacting with the scalar field. The other two more compact models collapse to a black hole instead on a dynamical time scale. The dashed lines are taken from our evolutions of the equilibrium model without the presence of the scalar field.

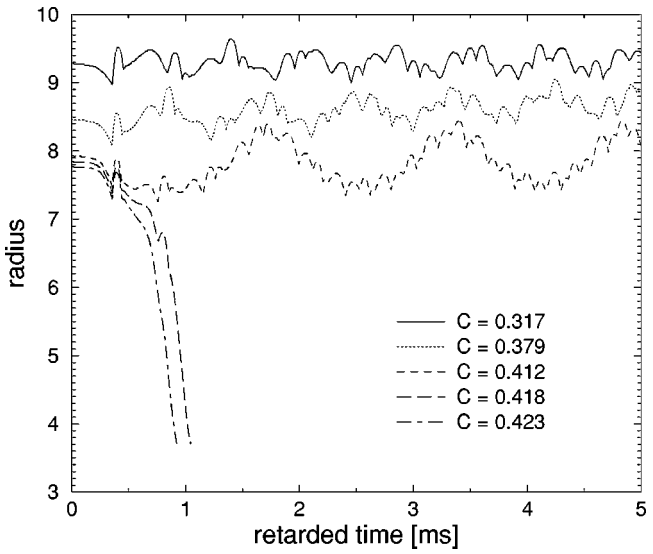

FIG. 7. Time evolution of the radius of the different relativistic stars interacting with the scalar field. The radius of the two most compact models decreases dramatically, indicating that they undergo gravitational collapse to a black hole.

threshold of black hole formation, the amplitude of the oscillations is big enough to show nonlinear effects, the oscillation frequency being much smaller than the value obtained from linear studies. For the models with central densities of $\rho_c = 2.9\times10^{-3}$ and 3.0×10^{-3} the interaction with the scalar field is able to trigger their gravitational collapse to a black hole on a dynamical time scale. Unfortunately, due to numerical inaccuracies arising at the end of the simulation we are not able to follow the collapse process once the event horizon is about to form (similar problems were reported in [27] for the collapse of supermassive stars). However, convergence studies show clear evidence that these models collapse to black holes. Further evidence is given by the evolution of the relativistic star radii, as shown in Fig. 7, and the blow-up of the redshift between the stellar center and future null infinity. We have plotted in Fig. 8 the redshift factor e^{2H} relating the lapse of local proper time at the origin to the lapse of proper time at infinity according to Eq. (7). For example, for the model with central density $\rho_c = 2.9\times10^{-3}$, initially, the redshift factor e^{2H} between the center of the star and observers located at $r\to\infty$ is 2.1. By the end of the simulation it has increased to a value of 59.5. This high redshift factor explains the appearance of a kink in the central density toward the end of our numerical evolution (see Fig. 6). We note that global energy conservation is well maintained, even for these extreme hydrodynamic simulations. The relative deviation from energy conservation according to Eq. (23) when the evolution stops is of the order of 10^{-4}.

By analyzing the energy transfer from the scalar field to the relativistic star during the interaction we find that it increases with the compactness of the stellar model. This behavior is shown in Table II. We remark that the initial mass of the scalar field is not strictly the same in all cases considered, due to the different underlying geometry on which the initial scalar field data are set. We evaluate the total radiated mass in the scalar field at a retarded time of $\tau = 0.6$ ms. The mass radiated away to infinity after this time is negligible.

Next we analyze the behavior of the scalar field in these scattering simulations. In Fig. 9 we plot the (retarded) time evolution of the news, Eq. (22), for the whole sample of our star models. The scalar field signal measured at null infinity can be divided into three phases. The first phase, before the main pulse reflects off the origin (not shown in the figure) is

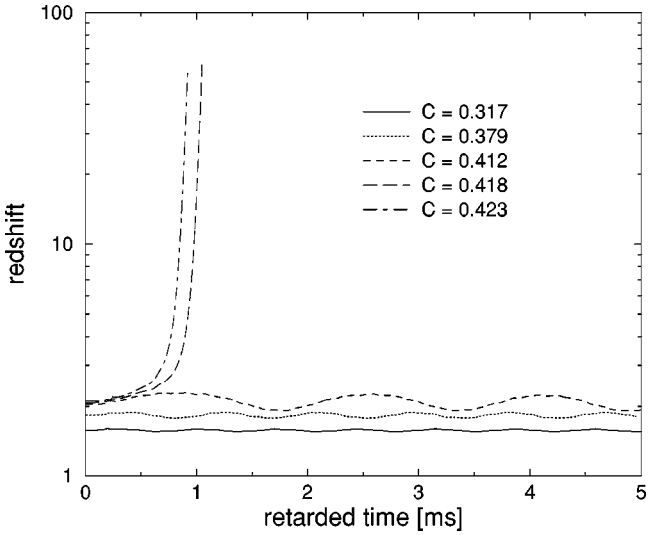

FIG. 8. Time evolution of the redshift factor e^{2H} relating the lapse of proper time at the origin to the lapse of proper time at infinity according to Eq. (7). The rapid increase in the redshift factor for the two most compact models gives clear evidence for the formation of black holes.

TABLE II. Energy transfer from the scalar field to the relativistic star during the scattering process. The entries are as follows: ρ_c is the central density of the relativistic star, M_0^Φ is the initial mass of the scalar field, $E_{\rm rad}$ is the total radiated mass, and $E_{\rm trans}$ is the percentage of the energy transferred in the interaction. We use units in which $G=c=M_\odot=1$.

ρ_c (10^{-3})	M_0^Φ (10^{-3})	$E_{\rm rad}$ (10^{-3})	$E_{\rm trans}$ (%)
1.5	4.90	4.86	0.8
2.2	4.80	4.72	1.7
2.8	4.76	4.65	2.3
2.9	4.75	4.63	2.5
3.0	4.75	4.62	2.7

dominated by an initial backscattering with small signal amplitude. The second phase, whose duration depends on the compactness of the relativistic star [26], is characterized by the reflection of the main scalar field back and forth between the origin and the maximum of the relativistic star curvature potential, which, in turn, induces the appearance of quasinormal oscillations on the scalar field. Most of the energy is radiated away in this period. Once the pulse has lost sufficient energy it enters a third phase, during which the behavior of the signal is dominated by a power-law tail $N\propto t^{-\alpha}$, with $\alpha=3$, due to the reflection of the scalar field at the exterior Schwarzschild geometry [21,17,18,26]. Since the compactness of our models is well below the Buchdahl limit $C=8/9$, the quasinormal mode ringing phase does not last for an extended period of time. Therefore, after a few reflections trapped inside the curvature potential, the signal rapidly enters the power-law tail phase. From Fig. 9 one can see that the more compact the relativistic star, the larger the quasi-

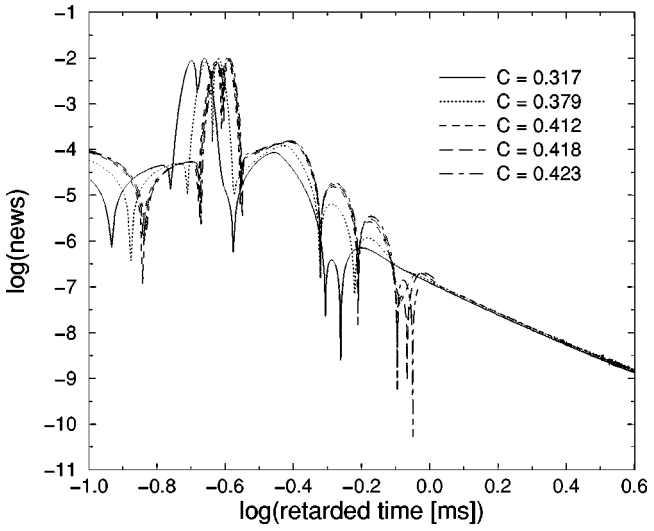

FIG. 9. Time evolution of the news function during the scattering problem. The different lines correspond to the different models in our sample of Table I, and are labeled in the plot with respect to the compactness parameter. The duration of the more dynamic quasinormal ringing phase strongly depends on the compactness of the relativistic star model, increasing as the compactness increases. The late time behavior of the signal decays as an inverse power law.

TABLE III. Late time power-law behavior of the news $N\propto t^{-\alpha}$ for the (stable) relativistic star—scalar field scattering problem. The results agree with the value $\alpha=3$ predicted by linear theory.

ρ_c (10^{-3})	α
1.5	3.06
2.2	3.05
2.8	3.05

normal ring-down phase. We also point out that by going to more compact models, increasing the central density of the relativistic star beyond the maximum of the stability curve (i.e., going into the unstable branch) and freezing the hydrodynamics and metric evolution to avoid gravitational collapse, we are able to find a much longer ring-down phase. Our results, obtained for fully self-gravitating, polytropic relativistic star models, are in good agreement with previous findings by Pavlidou *et al.* [26], who used a more idealized setup consisting of constant density, static stars.

The study of the late time power-law tails requires increased resolution, especially for large radii; hence we have used a different radial coordinate for these simulations, $r=30x/(1-x^4)$. This allowed us to resolve the power-law behavior in Fig. 9, preventing the evolution from being dominated by numerical noise mainly due to reflections. By performing a linear regression study of the tails in the time interval $\log(\tau\,[\mathrm{ms}])\in[0.3;0.7]$, we obtain the results summarized in Table III. We find the correct power-law behavior of the scalar field in our fully dynamical evolutions, as predicted by both linear analysis and nonlinear numerical evolutions of scalar fields in the exterior black hole geometry [17–19]. Note that we measure the tails on the news, whereas the results of the above references read off the quantity g at future null infinity $\mathcal{J}^+$. The two quantities are related by

$$N=e^{-2H}g_{,u}. \tag{28}$$

VI. SUMMARY

We have analyzed numerically the interaction of relativistic stars and scalar fields by means of nonlinear evolutions of the Einstein-Klein-Gordon perfect fluid system in spherical symmetry. We have built a sequence of stable, self-gravitating, $K=100$, $n=1$ relativistic polytropes, increasing the central density from $\rho_c=1.5\times10^{-3}$ to 3.0×10^{-3} ($G=c=M_\odot=1$). Using a compactified spacetime foliation with outgoing null cones we have studied the fate of the relativistic stars when interacting with a sufficiently strong scalar field wave packet, as well as the dynamics and energetics of the process.

We have found that by choosing a strong (finite amplitude) scalar field pulse with energy of the order of $10^{-3}M_\odot$, the relativistic star is forced either to oscillate in its radial modes of pulsations or to collapse to a black hole on a dynamical time scale. The fate of the star depends on its central density and, since we fix the polytropic equation of state, on its compactness. The energy transferred to the relativistic star

increases with increasing compactness of the model. The radiative signals we have found in our fully nonlinear simulations consist of several quasinormal oscillations and a late time power-law tail, in agreement with the results predicted by (linear) perturbation analysis of wave propagation in an exterior Schwarzschild geometry [21].

ACKNOWLEDGMENTS

It is a pleasure to thank Ewald Müller for useful discussions and for a careful reading of the manuscript, and Johannes Ruoff for kindly providing us the frequencies of the fundamental modes of the neutron star models of Sec. IV A, obtained with his perturbation code. We further thank Nigel Bishop and Carsten Gundlach for helpful comments on the manuscript. F.S. would like to thank the Relativity and Cosmology Group of the University of Portsmouth, where part of this work was completed. This work was supported, in part, by the EU Program ''Improving Human Research and the Socio-Economic Knowledge Base'' (Research Training Network Contract HPRN-CT-2000-00137). P.P. also acknowledges support from the Nuffield Foundation (Grant No. NAL/00405/G).

[1] C. L. Fryer, D. E. Holz, and S. A. Hughes, astro-ph/0106113.
[2] R. F. Stark and T. Piran, Phys. Rev. Lett. **55**, 891 (1985).
[3] M. Shibata, Prog. Theor. Phys. **104**, 325 (2000).
[4] H. Dimmelmeier, J. A. Font, and E. Müller, Astrophys. J. Lett. **560**, L163 (2001).
[5] H.-Th. Janka, K. Kifonidis, and M. Rampp, in *Proceedings of the Workshop on Physics of Neutron Star Interiors*, edited by D. Blaschke, N. K. Glendenning, and A. D. Sedrakian (Springer, Berlin, in press), astro-ph/0103015.
[6] E. Müller, in *Computational Methods for Astrophysical Fluid Flow*, edited by O. Steiner and A. Gautschy (Springer-Verlag, Berlin, 1998), pp. 343–494.
[7] H. Bondi, M. G. J. van der Burg, and A. W. K. Metzner, Proc. R. Soc. London **A269**, 21 (1962).
[8] R. K. Sachs, Proc. R. Soc. London **A270**, 103 (1962).
[9] L. A. Tamburino and J. H. Winicour, Phys. Rev. **150**, 1039 (1966).
[10] R. A. Isaacson, J. S. Welling, and J. Winicour, J. Math. Phys. **24**, 1824 (1983).
[11] J. Winicour, Living Rev. Relativ. **4**, 3 (2001).
[12] R. Gómez, P. Papadopoulos, and J. Winicour, J. Math. Phys. **35**, 4184 (1994).
[13] P. Papadopoulos and J. A. Font, Phys. Rev. D **61**, 024015 (2000).
[14] P. Papadopoulos and J. A. Font, Phys. Rev. D **63**, 044016 (2001).
[15] R. Gómez and J. Winicour, J. Math. Phys. **33**, 1445 (1992).
[16] R. L. Marsa and M. W. Choptuik, Phys. Rev. D **54**, 4929 (1996).
[17] C. Gundlach, R. H. Price, and J. Pullin, Phys. Rev. D **49**, 883 (1994).
[18] C. Gundlach, R. H. Price, and J. Pullin, Phys. Rev. D **49**, 890 (1994).
[19] R. Gómez, J. Winicour, and B. Schmidt, Phys. Rev. D **49**, 2828 (1994).
[20] P. Papadopoulos and P. Laguna, Phys. Rev. D **55**, 2038 (1997).
[21] R. H. Price, Phys. Rev. D **5**, 2419 (1972); **5**, 2439 (1972).
[22] S. H. Hawley and M. Choptuik, Phys. Rev. D **62**, 104024 (2000).
[23] K. D. Kokkotas and B. G. Schmidt, Living Rev. Relativ. **2**, 2 (1999).
[24] G. Allen, N. Andersson, K. D. Kokkotas, and B. F. Schutz, Phys. Rev. D **58**, 124012 (1998).
[25] J. Ruoff, Phys. Rev. D **63**, 064018 (2001).
[26] V. Pavlidou, K. Tassis, T. W. Baumgarte, and S. L. Shapiro, Phys. Rev. D **62**, 084020 (2000).
[27] F. Linke, J. A. Font, H. T. Janka, E. Müller, and P. Papadopoulos, Astron. Astrophys. **376**, 568 (2001).
[28] R. Gómez, J. Winicour, and R. Isaacson, J. Comput. Phys. **98**, 11 (1992).
[29] L. Lehner, J. Comput. Phys. **149**, 59 (1999).
[30] B. van Leer, J. Comput. Phys. **32**, 101 (1979).
[31] A. Harten, P. D. Lax, and B. van Leer, SIAM Rev. **25**, 35 (1983).
[32] B. Einfeldt, SIAM (Soc. Ind. Appl. Math.) J. Numer. Anal. **25**, 294 (1988).
[33] J. A. Font, Living Rev. Relativ. **3**, 2 (2000).
[34] J. A. Font, M. Miller, W.-M. Suen, and M. Tobias, Phys. Rev. D **61**, 044011 (2000).
[35] J. A. Font, N. Stergioulas, and K. D. Kokkotas, Mon. Not. R. Astron. Soc. **313**, 678 (2000).
[36] J. Ruoff (private communication).